Temperature dependent spin momentum densities in Ni-Mn-In alloys

B L Ahuja[1], Alpa Dashora[1], N L Heda[2], K R Priolkar[3], L Vadkhiya[1], M Itou[4], Nelson Lobo[3], Y Sakurai[4], Aparna Chakrabarti[5], Sanjay Singh[6], and S R Barman[6]

[1] Department of Physics, University College of Science, M. L. Sukhadia University, Udaipur 313001, India
[2] Department of Pure and Applied Physics, University of Kota, Kota 324005, India
[3] Department of Physics, Goa University, Goa 403206, India
[4] Experimental Research Division, Japan Synchrotron Radiation Research Institute, SPring8, Mikazuki, Hyogo 679-5198, Japan
[5] Raja Ramanna Centre for Advanced Technology, Indore 452013, India
[6] UGC-DAE Consortium for Scientific Research, Khandwa Road, Indore 452001, India.

E-mail: blahuja@yahoo.com (Prof. B L Ahuja)

Abstract

The spin-dependent electron momentum densities in Ni_2MnIn and $Ni_2Mn_{1.4}In_{0.6}$ shape memory alloy using magnetic Compton scattering with 182.2 keV circularly polarized synchrotron radiations are reported. The magnetic Compton profiles were measured at different temperatures ranging between 10-300 K. The profiles have been analyzed mainly in terms of Mn 3d electrons to determine their role in the formation of the total spin moment. We have also computed the spin-polarized energy bands, partial and total density of states, Fermi surfaces and spin moments using full potential linearized augmented plane-wave and spin polarized relativistic Korringa-Kohn-Rostoker methods. The total spin moments obtained from our magnetic Compton profile data are explained using both the band structure models. Present Compton scattering investigations are also compared with magnetization measurements.

(Some figures in this article are in colour only in the electronic version)

PACS number (s): 75.50.Cc, 83.85.Hf, 75.20.Hr, 75.25.+z

Keywords: Magnetic Compton scattering, Spin momentum density, Heusler alloys, Electronic structure calculations.

1. Introduction

The ferromagnetic Ni_2MnIn belongs to the class of Heusler alloys with general composition X_2MnY (X = Co, Ni, ….., and Y = Al, Ge, Si, In, Sn, …..). Recently, Ni-Mn-In (Sn, Sb) series has attracted much attention because of unique properties of these alloys owing to shape memory effect, giant magnetocaloric effect, large magnetoresistance and other interesting magnetic properties such as the coupled magnetic-martensitic transformation [1]. The electronic structure of X_2MnY alloys was predicted to significantly depend on the type of element Y due to the hybridization between d states of Mn and p states of Y [2]. These alloys show magneto-structural phase transitions and are suitable for the semiconductor spintronics devices. Da Silva *et al* [3] have reported the electronic structure of Ni_2MnIn using linear muffin-tin-orbital (LMTO) method. Kilian and Victora [4] have presented the minority- and majority-spin band structures along with the magnetic moments using linearized augmented Slater type orbitals (LASTO) and compared their results with the Da Silva *et al* [3]. Godlevsky and Rabe [5] have examined the energy bands, density of states (DOS) and magnetic moment of Ni_2MnIn using first principle local spin density (LSD) pseudopotential calculations. The inter-sublattice exchange interactions and Curie temperature (T_C) in Heusler alloys Ni_2MnX (X = Ga, In, Sn and Sb) were studied within the framework of the density functional theory (DFT) by Şaşioğlu *et al* [6]. The magnetic, magneto-optical and optical properties of Ni_2MnIn were investigated by Kudryavtsev *et al* [7]. They have also shown that crystalline Ni_2MnIn films were ferromagnetic with a T_C of 325-330 K while the amorphous phase was not ferromagnetically ordered down to 5 K. The first-principles calculations [8, 9] were used to describe the electronic structure, magnetic properties and

phonon anomalies in Heusler alloys like Ni_2MnIn, Mn_2NiIn, $NiMnGa_2$, Ni_2MnAl, Ni_2MnGa, Ni_2MnGe and Mn_2NiGa. The structure of Ni_2MnGa was reported to have modulation [10] that was related to low twinning stress that leads to magnetic field induced strain [11]. Yablonskikh *et al* [12] have reported the magnetic and chemical bonding effects using soft X-ray spectroscopy. The authors have also computed magnetic moments using full potential linearized augmented plane wave method (FP-LAPW) within generalized gradient approximation (GGA). Buchelnikov *et al* [13] have reported the complex temperature dependence of magnetization of Ni-Mn-*X* (*X* = In, Sn and Sb) on the basis of Monte Carlo simulation using the Potts model Hamiltonian. Krenke *et al* [14] have measured the temperature and magnetic field dependent magnetization of $Ni_2Mn_{1+x}In_{1-x}$ ($0.0 \leq x \leq 0.8$) using a superconducting quantum interference device (SQUID) magnetometer. The authors have discussed the shape memory effects at different values of *x*. Recently, Kanomata *et al* [15] have measure the magnetization of $Ni_2Mn_{1+x}In_{1-x}$ ($0.0 \leq x \leq 0.6$) using a commercial SQUID magnetometer. Interestingly, at 5 K, the values of the magnetic moment for samples with $0.368 \leq x \leq 0.408$ were found to be much smaller than samples with $0.0 \leq x \leq 0.32$. At 5K, the magnetization results of Kanomata *et al* [15] for $x=0.40$ disagree with the magnetization data of $Ni_2Mn_{1.34}In_{0.66}$ reported by Krenke *et al* [14]. Therefore, to optimize the functional properties, a proper focus on the magnetic properties employing a reliable technique like magnetic Compton scattering is required.

Magnetic Compton profile (MCP), $J_{mag}(p_z)$, is defined as the one-dimensional projection of spin-polarized electron momentum density [16-18]. It is given as

$$J_{mag}(p_z) = \iint \rho_{mag}(\boldsymbol{p})\, dp_x\, dp_y, \tag{1}$$

$$\rho_{mag}(\boldsymbol{p}) = \left|\chi_{\uparrow}(\boldsymbol{p})\right|^2 - \left|\chi_{\downarrow}(\boldsymbol{p})\right|^2, \tag{2}$$

where $\chi_{\uparrow(\downarrow)}(\boldsymbol{p})$ corresponds to the momentum wave function of an occupied majority (minority) spin state and p_z is the component of electron linear momentum along the z-axis. Moreover, z-axis is parallel to scattering vector **k** (**k**=$\mathbf{k}_1 - \mathbf{k}_2$; where $\mathbf{k}_1$ and $\mathbf{k}_2$ being the wave vectors of incident and scattered X-rays).

The area under Compton line, $\int J_{mag}(p_z)dp_z$, is equal to the total spin moment per formula unit (μ_{spin}) in Bohr magnetons.

In the present work, atomic units (a.u.) are used, where 1 a.u. of momentum is = 1.99 x 10^{-24} kg m s^{-1}. In the magnetic Compton scattering (MCS), the profile is difference of the two spectra, collected sequentially for two opposite magnetization directions of the target. The magnetic effect (*R*), which is proportional to the net spin moment μ_{spin}, is expressed as

$$R = \frac{I^A - I^B}{I^A + I^B} \propto \mu_{spin}, \qquad (3)$$

where I^A and I^B are the integrated Compton intensities of scattered photons for the magnetization being parallel and antiparallel to **k**, respectively. The ratio *R* corresponds to the ratio of magnetic to charge intensities.

Regarding spin momentum densities of Heusler alloys, Zukowski *et al* [19] have reported the experimental MCP of Cu-Mn-Al system. Deb and Sakurai [20] have also computed the MCPs of Cu_2MnAl using FP-LAPW method within local spin density approximation (LSDA) and GGA. The experimental MCPs of Co_2FeGa and Ni_2MnSn were also studied by Deb *et al* [21, 22], in which they have shown the negative spin polarization of the conduction electrons. Recently, Ahuja *et al* [23] have reported the MCS study of Ni and

Mn-rich Ni-Mn-Ga alloys and the data have been discussed in terms of the Mn 3d and Ni 3d delocalized spin moments.

In this paper, we report the MCPs of Ni_2MnIn and $Ni_2Mn_{1.4}In_{0.6}$ at different temperatures (10, 175 and 300 K) using circularly polarized synchrotron radiations at SPring8, Japan [18]. For the computation of electronic and magnetic properties, we have also employed FP-LAPW and spin polarized relativistic Korringa-Kohn-Rostoker (SPR-KKR) schemes. The aim of present measurements is multifold, namely (a) to measure the first ever temperature dependent spin momentum density of Ni-Mn-In system (b) to check the magnetic transitions in a wide range (10-300 K) of temperature (c) to check the role of Mn 3d electrons in formation of total spin moments (d) to compare and analyze the data in terms of band structure calculations using FP-LAPW and SPR-KKR schemes and (e) to compare the results of MCP and band structure calculations with the existing controversial magnetization data.

2. Experiment

Bulk polycrystalline ingot of nominal compositions Ni_2MnIn and $Ni_2Mn_{1.4}In_{0.6}$ were prepared by arc melting technique using appropriate quantities of Ni, Mn and In in an argon atmosphere. After ensuring the homogeneity, these were annealed at 750^oC for 48 hours in evacuated sealed quartz tube and subsequently quenched in ice-cold water. The composition of the Ni_2MnIn and $Ni_2Mn_{1.4}In_{0.6}$ specimen were determined by energy dispersive analysis of x-rays (EDAX) using scanning electron microscope. EDAX has been performed by estimating the intensities of Ni-, Mn- and In- K_α characteristic lines (5.9-9.2 keV), which were well separated and have small background. On averaging over several measurements (eight different spots on the specimen), the sample compositions

turned out to be $Ni_{2.02}Mn_{1.05}In_{0.92}$ and $Ni_{2.03}Mn_{1.35}In_{0.64}$. The powder X-ray diffraction patterns of Ni_2MnIn and $Ni_2Mn_{1.4}In_{0.6}$ are shown in figures 1 (a-b). We fitted both the XRD patterns with both Rietveld and Le Bail fitting procedures [24, 25]. The Ni_2MnIn shows cubic $L2_1$ structure at room temperature (RT) with lattice parameter a= 6.0537 Å. The non-stoichiometric specimen $Ni_2Mn_{1.4}In_{0.6}$ can be indexed also by $L2_1$ phase, along with a small amount of martensite phase with tetragonal structure (about 13%, as estimated by Rietveld fitting). There is no possibility of CsCl-type phase in any of the present samples since if we use CsCl type (B2) cubic structure with smaller lattice parameter a≈ 3 Å to fit the XRD patterns, the peaks situated at angles 2θ= 25.61° (1 1 1), 50.23° (1 1 3) and 67.81° (3 1 3) cannot be indexed. These peaks are associated with the $L2_1$ structure. The Le Bail fitting as well as the indexing are shown in figures 1 (a-b). The (1 1 1) and (1 1 3) peaks are also shown in inset of figure 1 (a) in an expanded scale. From fitting of the XRD data this is clear that both samples have ordered $L2_1$ structure in the cubic phase.

For $Ni_2Mn_{1.4}In_{0.6}$ at RT, the peaks corresponding to the small amount of the tetragonal martensitic phase are indicated by 'T' in the figure 1 (a). The tetragonal phase at RT can be due to fact that the martensitic transition temperature of this sample is close to RT (270 K) [26]. Since the sample has not been annealed after grinding it into powder, the residual stress induced by the grinding process can induce martensitic phase at temperature higher than the martensitic transition temperature. Such stress induced tetragonal phase has recently been observed in the RT XRD of Mn_2NiGa [27].

The temperature dependent MCP measurements on both the polycrystalline samples have been carried out in the reflection geometry using the magnetic Compton spectrometer at

the high energy inelastic scattering beam line BL08W at SPring-8 (Super photon ring 8 GeV), Japan [16, 18]. During the measurements, the peak brightness of elliptical multipole wiggler was 1.378 x 10^{17} phs^{-1} $mrad^{-2}$ mm^{-2} per 0.1 % bandwidth with a critical energy 42.6 keV. The incident X-rays of energy 182.2 keV with elliptically polarized component (P_c=0.55) were selected using a Johann-type Si (620) monochromator. The beam size at the sample position was limited to 0.8 mm (h) x 0.8 mm (w). The resolution (Gaussian, full width at half maximum) of the spectrometer was 0.40 a.u. The energy dispersive detection system, which was used to analyze the Compton spectra, consisted of ten Ge elements with individual spectroscopy amplifiers, analog to digital converters and multi-channel analyzers. The Ge crystals (each 100 mm^2 cross-section) were circularly arranged around a hole (11 mm diameter) to collect the scattered photons. The distances between detector-sample and monochromator-sample were 1 and 13.1 m, respectively. A super-conducting magnet was used to apply the magnetic field in the sample in the sequence of ABBAABBA…….. where A and B represent the relative direction of the magnetic field and the scattering vector [A being parallel and B antiparallel]. A switching time of 1 s and a dwell time of 60 s were used to ensure good signal averaging. The back-scattered raw MCP data were corrected for the energy dependence of the detector efficiency, absorption and the relativistic cross-section corrections. The correction for the multiple scattering was neglected, as the spin dependent multiple scattering is always very small [18, 23]. The data were then converted from energy to momentum scale. Finally, the Compton profiles were normalized to spin moment per formula unit. The normalization of the experimental magnetic Compton profiles was determined using the

R (defined in Eq. 3) of standard Fe sample. The total unknown spin moment of Ni-Mn-In samples (μ^S) was calculated from the relation

$$\mu^S = \mu^{Fe}\left(\frac{A^S R^S}{A^{Fe} R^{Fe}}\right), \quad (4)$$

where A is the number of electrons taking part in Compton scattering. The magnetic moment of Fe (μ^{Fe}) was taken as 2.16 μ_B. In the chosen momentum range –10 to +10 a.u., A^S (the integral of free atom Compton profile) was equal to 118.48 and 110.79 electrons for Ni_2MnIn and $Ni_2Mn_{1.4}In_{0.6}$, respectively. The A^{Fe} was equal to 24.32 electrons. To measure the R^{Fe}, a separate MCP run on the Fe sample was attempted. The R^{Fe} was found to be 0.019694.

To check the T_C and other magnetic transitions, a systematic temperature dependent magnetization M-T in low external field (H = 0.01 T) was also measured in the temperature range 5K $\leq T \leq$ 350K using a SQUID magnetometer. Prior to the measurements, the sample was zero-field cooled (ZFC) from 350 to 5K. At this point the magnetic field was applied and the magnetization was recorded for field heated (FH) and field cooled (FC) cycles.

3. Theory

To perform the band structure calculations, we have used FP-LAPW method as embodied in the Wien2k [28]. In this method, there are no shape approximations to the charge density or potential. Unlike pure Muffin-tin (MT) approximation, the choice of MT radii in full-potential calculations (where one looks at minimum charge density between two adjacent atoms) is not critical. The FP-LAPW is among the most accurate methods for performing electronic structure calculations for crystals. It is based on the DFT for the

treatment of exchange and correlation. In our calculations, the exchange-correlation potential was treated within LSDA (Perdew and Wang [29]) and the latest prescription of GGA as suggested by Wu and Cohen [30]. The muffin-tin radius (R_{MT}) used in the computation was 2.47, 2.47 and 2.40 a.u. for Ni, Mn and In, respectively. The value of $R_{MT}K_{max}$ for Ni_2MnIn was taken to be 9 (K_{max} is the maximum modulus of the reciprocal lattice vectors). The maximum radial expansion l_{max} was set to 10. The Brillouin zone integration was performed with 256 $\boldsymbol{k}$ (20x20x20) points in the irreducible wedge of the Brillouin zone (IBZ). In a separate calculation, we have seen that the incorporation of more $\boldsymbol{k}$ point in the IBZ does not affect the results of electronic or magnetic properties. The cutoff for the charge density was G_{max}=14. To ensure accuracy in convergence, the total energy of the crystal was converged to 0.01 mRy (default value). The optimized lattice constant (a= 6.0625 Å), which corresponds to the lowest total energy, was used in the present computations.

In case of $Ni_2Mn_{1.4}In_{0.6}$, we have computed the electronic structure using a super cell of dimension 2x2x2 leading to 32 atoms in the super cell. For the sake of clarity, Mn atoms at Mn sublattice are denoted by Mn(I). In the present computations for $Ni_2Mn_{1.375}In_{0.625}$ (hereafter referred as $Ni_2Mn_{1.4}In_{0.6}$), three In atoms in the super cell were replaced by Mn atoms which are named as Mn(II) in the forthcoming discussion. For sufficient accuracy within super cell computations, other governing parameters $R_{MT}K_{max}$, l_{max}, G_{max} and number of $\boldsymbol{k}$ points in the IBZ were set to 7, 10, 12 and 102, respectively.

The electronic properties and magnetic moments for both the Ni-Mn-In alloys were also computed self-consistently by means of the SPR-KKR method within the coherent potential approximation (CPA) [31]. The scheme is based on KKR Green's function

formalism, which makes use of multiple-scattering theory. This means that the electronic structure is not represented by means of Bloch wave functions and eigen energies but the electronic Green's function. In the present calculations, the l_{max} (the angular momentum expansion for the major component of the wave function) was restricted to 2. For self-consistent field cycles, 834 $\boldsymbol{k}$ points were generated by $\boldsymbol{k}$-mesh of {22, 22, 22}. To achieve the convergence, in our KKR calculations, we have used BROYDEN2 scheme (an iterative quasi-Newton method to solve the system of non-linear equations) with the exchange-correlation potential of Vosko-Wilk-Nusair (VWN) [32]. In order to achieve faster convergence, the SCF mixing parameter was set to 0.20. Since Wien2k and SPR-KKR codes do not facilitates the similar exchange and correlation, we have chosen different prescriptions in the FP-LAPW and SPR-KKR calculations as mentioned in theoretical part. Our experience guides us that the total value of spin moment computed using different schemes of exchange and correlation may differ up to 0.05 μ_B/f.u.

4. Results and discussion

The spin projected energy bands and DOS resulting from the FP-LAPW (LSDA) calculations of Ni-Mn-In are shown in figures 2-5. In case of Ni_2MnIn (figure 2), it is seen that the valence bands disperse between 0 and –10 eV (shown here upto –3 eV only). In both the minority- and majority-spin bands, it is observed that the energy bands cross the Fermi level (E_F) along various symmetry directions prohibiting the half-metallic like character of Ni_2MnIn. At Γ point, the majority-spin bands show large energy separation in comparison to minority-spin bands that are nearly flat close to E_F and are related to Ni 3d-Mn 3d hybridized states. In figure 3, we have presented the total and partial spin-resolved DOS. An individual contribution of 3d states (e_g and t_{2g}) is also

highlighted in the DOS curves. In the majority-spin DOS, Mn 3d states show the maximum contributions in the vicinity of –1 and –3 eV, while Ni 3d states have maximum contribution between −1 and −2 eV. It is also found that in case of majority-spin valence states; the 3d bands of Ni and Mn atoms overlap with each other and are mostly occupied. In contrary, for the minority-spin states, the main contribution arises from the Ni 3d states, while the Mn 3d states have hardly any contribution. The minority-spin Mn 3d states appear above E_F with the peak around 1.5 eV. Thus, while the unoccupied states are dominated by Mn 3d minority-spin states, the occupied part have larger contribution from both majority and minority Ni 3d hybridized with majority-spin Mn 3d states. This is the reason for large local moment in Mn that is the characteristic of Heusler alloys. On the contrary, the net magnetic moment on Ni atoms is small that is understandable in terms of cancellation of spin dependent DOS in minority- and majority-spins.

The electron states obtained from the SPR-KKR are similar to FP-LAPW, except some fine structures and small shifts in the bands. Worth mentioning is the position of the Mn 3d minority-spin peak in the unoccupied DOS: it appears at 0.5 eV in KKR, in contrast to FP-LAPW where it appears at 1.5 eV. Experimentally, Mn 3d peak in the unoccupied DOS from inverse photoemission spectroscopy for a related compound Ni_2MnGa has been reported at 2 eV [33]. Thus, FP-LAPW provides a better description of the unoccupied states compared to SPR-KKR.

In case of $Ni_2Mn_{1.4}In_{0.6}$ (figure 4), the number of bands is 8 times than that of Ni_2MnIn because of large size of unit cell. Unlike Ni_2MnIn, several bands cross the E_F level in all the branches. The spaghetti of bands between –0.5 to –4.0 eV are related to hybridization

between Mn 3d–Ni 3d states. A small contribution of In (5s and 5p) states are seen from the majority- and minority-spin bands. In figure 5, from the majority-spin DOS, it is seen that Mn(I) and Mn(II) are coupled antiferromagnetically, canceling each other contribution. Due to these cancellation effects, the resultant moment at Mn site and hence the total spin moment is reduced. Using FP-LAPW calculations, the calculated magnetic moments at individual sites with multiplicity of the atoms are presented in table 1. As seen in DOS curves also, the magnetic moments at Mn(I) and Mn(II) sites are opposite in direction. It shows that the coupling between Mn magnetic moments is altered from ferromagnetic alignment when Mn atoms occupy the In site in non-stoichiometric $Ni_2Mn_{1.4}In_{0.6}$ alloy.

The theoretical spin moments computed by us using different exchange and correlation schemes of FP-LAPW and SPR-KKR methods (table 2) are found to be in reasonable agreement with the available data [3-6, 9, 12]. It is worth mentioning that the LSDA is based on slowly varying spin densities. In comparison to LSDA, GGA tend to improve total energies, energy barriers and structural differences, etc. It also corrects or some times overcorrect the LSDA prescriptions. On the other hand the CPA (KKR-CPA) which treats the disordered effects within the frame work of MT Hamiltonian provides charge and spin-self consistent parameters, electronic structure and properties of complicated materials possessing many atoms in unit cell. A comparison with the experimental data is discussed at later stage.

In figure 6 (a) the standard BZ for $L2_1$ structure labeled with high symmetry points is presented. The Fermi surfaces (FS) due to majority- and minority-spin electrons for Ni_2MnIn are shown in figures 6 (b-i). The FS drawn in figure 6 (b) are due to 31^{st} band in

majority-spin (marked in figure 2a) within the energy range –0.66 to 4.89 eV. It reproduces a rounded octahedron around Γ point due to holes. The 32nd and 33rd bands also contribute in almost same energy range (–0.57 to 4.88 eV). The hole like FS (figure 6c) arising due to 32nd band have eight branches which are in touch with the hexagonal faces of BZ around *L* points. The FS due to 33rd band have star like hole structure (figure 6d) around the *K* points which cover the square surfaces of BZ. Figure 6 (e) shows the complete mapping of FS from majority-spin bands. The FS formed by minority-spin bands are shown in figures 6 (f-h). The 26th band (–1.30 to 0.08 eV) leads to a small octahedron (hole) at Γ point as shown in figure 6 (f). The next minority-spin band (27th band) in the energy range –0.60-0.41 eV gives cone like structures combining at Γ point. More over, the open side of cones touches at the hexagonal surface of the BZ around *L* point. The FS shown in figures 6 (d) and 6 (h), which are due to part of 3d electrons of Ni, are almost similar. Therefore, contribution of Ni 3d states in the magnetic properties of Ni_2MnIn is very small. Total FS due to minority-spin structures is shown in figure 6 (i). The different shapes of majority- and minority-spin FS (figures 6 e, i) also support the origin of the magnetization in Ni_2MnIn.

The variation of the magnetic effect *R* with temperature (at 2.5 T field) and our SQUID based low field (0.01 T) magnetization data are shown in figures 7 (a-b). Our limited data depicts a significant decrease in *R* at room temperature which is consistent with the T_C (314 K for Ni_2MnIn and 306 K for $Ni_2Mn_{1.4}In_{0.6}$). Magnetization data of $Ni_2Mn_{1.4}In_{0.6}$ at low field clearly show magnetic transitions (austenitic/martensitic) below 250 K. It is worth noting that the magnetic Compton scattering experiment are performed at high field (at saturated magnetization), therefore the transitions seen in low field may not be

visible during high field measurements, as seen in figure 7 b also. As is known, the magnetic Compton scattering is sensitive to the spin moments arising from the superposition of contribution from different unpaired electrons. MCP provides magnetic moment at different local sites by splitting the $J_{mag}(p_z)$ into its individual components [16, 18, 23]. To incorporate the individual magnetic contribution of the Mn 3d, Ni 3d and diffuse (s, p-like itinerant) electrons, we have fixed the contribution of Ni 3d electrons because the free atom profiles [34] of Mn 3d and Ni 3d at experimental resolution of 0.4 a.u. are not easily differentiable. The Ni local moment was kept fixed at the theoretical value obtained from present FP-LAPW data. As functions of temperature, the Ni moments have been changed proportional to the experimentally determined total magnetic moment. The variation of Ni moment at different temperatures is estimated with a simple model assuming that the contribution of Ni moment in formation of total spin moment is small and remains almost same. This is partly supported by values of Ni moments at different compositions, collated in table 1. Therefore, to a good approximation, the variation in Ni spin moment, is going to small with respect to temperature also. This model was also used in our earlier work on Ni-Mn-Ga system [23]. To separate out the MCP contribution of Ni, we have taken the spherical average of LSDA based magnetic Compton profile of Ni [35]. For the diffuse electrons, the parabolic Compton profile can be given by $J(p_z) = a_0 p_z^2 + a_1$ for $p_z < p_F$ and 0 for $p_z \geq p_F$ where constants a_0 and a_1 are the functions of number of free electrons and Fermi momentum (p_F). Our experience in the analysis of MCPs guides us that in such measurements the central dip (volcano structure) in the MCP can be fairly well approximated by an inverted parabola corresponding to diffuse components [23]. In the

present work, to model the contribution of the diffuse component (Mn 4s and In 5s, 5p), we have constructed equivalent Gaussian profile of full width at half maximum (FWHM) of 1.33 and 1.30 a.u., which corresponds to the respective FWHM of free electron Compton profile of the specimens Ni_2MnIn and $Ni_2Mn_{1.4}In_{0.6}$. All these profiles have been convoluted by a Gaussian FWHM of 0.4 a.u. to incorporate the effect of instrumental smearing.

Figures 8 (a)-(b) show the MCPs of both the Ni-Mn-In alloys for different temperatures 10, 175 and 300 K, splitted into individual components to yield the partial profile whose sum was the best fit to the data. In figures 9 (a-b), the temperature dependent spin moments derived from the area under curve of individual profiles at different temperatures (figure 8) are shown.

From figure 9 (a) it is evident that at the saturation field 2.5 T, the contribution of Mn 3d in Ni_2MnIn decreases with increasing the temperature. At all the temperatures, the Mn 3d contribution dominates in the formation of total spin moments. The diffuse contribution is anti-ferromagnetically coupled to Mn 3d and Ni contributions. Directly from the MCP data, we find the total spin moment to be 3.86 μ_B, while the Mn moment is 3.6 μ_B at the lowest possible temperature 10 K and 2.5 T. The total spin moment is in very good agreement with the saturation moment obtained from our SQUID magnetization data (3.85μ_B). Other SQUID based magnetization data [14, 15] are also closer to our MCP data. When compared with theoretical calculations, we find that Mn local moment obtained from MCP data is in very good agreement with the FP-LAPW (GGA) result of 3.59μ_B, while FP-LAPW (LSDA) value is slightly smaller (3.50μ_B). The Mn moment obtained from SPR-KKR is even smaller (3.42μ_B). Thus, FP-LAPW (GGA) gives the

best agreement with experimental data. However, the total spin moment 4.19 μ_B from FP-LAPW (GGA) is higher than that obtained from the MCP data (3.86μ_B). Our FP-LAPW data are in very good agreement with the previous magnetization (SQUID) reported by Krenke *et al* [14] and Kanomata *et al* [15]. The reason for lower total moment compared to theory (FP-LAPW) could be related to presence of excess Mn, the actual composition of the specimen being $Ni_{2.02}Mn_{1.05}In_{0.92}$. The spin moment of the excess Mn atoms can be antiferromagnetically aligned with the spin moments of the existing Mn atoms as discussed later.

In figure 9 (b), we present the MCP data at 10, 175, 300 K and our temperature dependent (1 T field) magnetization data for $Ni_2Mn_{1.4}In_{0.6}$. It is seen that our experimental value of total spin moment 3.10 μ_B/f.u. (at 10 K and 2.5 T field) is in close agreement with the ferrimagnetic SPR-KKR calculations. Our limited MCP data is also in good agreement with our SQUID data. The peculiar feature in our SQUID magnetization in the temperature range 200-300 K is due to martensitic transformation which remains even after application of high magnetic field. The present FP-LAPW (LSDA/GGA) calculations (2.65/2.62 μ_B/f.u.) for ferrimagnetic solution underestimate the total spin moment in comparison to MCP data (3.10 μ_B/f.u.). The total spin moment derived from the SPR-KKR data (3.21 μ_B/f.u.) is found to be closer to the MCP data. The overall contribution of Mn (3d) electrons in $Ni_2Mn_{1.4}In_{0.6}$ is less than that of Ni_2MnIn and also decreases with increasing the temperature. This happens because the spin moments of the excess Mn atoms are antiferromagnetically aligned with the spin moments of the existing Mn (as seen in table 1). This mechanism, which also explains the lower value of total spin moment in $Ni_{2.02}Mn_{1.05}In_{0.92}$, has indeed been suggested for non-stoichiometric

Ni-Mn-In to explain its inverse magnetocaloric behavior [36]. For a related compound with excess Mn ($NiMn_2Ga$ or Mn_2NiGa), it has been shown theoretically that the two Mn atoms are oppositely aligned leading to a ferrimagnetic ground state [37, 38]. The present MCP measurements and band structure calculations on non-stoichiometric composition confirm this explanation. A reasonable agreement between our magnetization and MCP data predict that the orbital moment in Ni-Mn-In system is very small, since MCP data only provides the contribution from the spin moments.

It is very interesting to note that the total spin moments derived from our Compton profile data, present magnetization curve and both the band structure calculations (FP-LAPW and SPR-KKR) are in reasonable agreement (figure 9b). On the contrary, in figure 9 (b), the total spin moment found in our $Ni_2Mn_{1.4}In_{0.6}$ (actual composition $Ni_{2.03}Mn_{1.35}In_{0.64}$) sample lies between the data reported by Kanomata *et al* [15] (1.41 μ_B/f.u.) for $Ni_2Mn_{1.4}In_{0.6}$ and by Krenke *et al* [14] (5.51 μ_B/f.u.) for $Ni_2Mn_{1.34}In_{0.66}$. The controversial values of spin moments may due to thermal history of specimens, as also reported in case of Ni-Mn-Ga system [33]. Krenke *et al* [14] have annealed their sample at 800°C for 2 h and then quenched it in ice water, while the Kanomata *et al* [15] have annealed the sample at 850°C for 3 days and quenched in water. In our case, as mentioned earlier, the subsequent homogenization of the ingot material was carried out by annealing the sample at 750°C for 48 h. Moreover, to check the large changes in magnetization due to thermal aspects during preparation, we have calculated the difference in total-energy between the ferro- and ferri-states using FP-LPAW (GGA) calculations. It is seen that the energy difference between ferro- and ferri-solutions is very small (0.0024 Ry) and the ferri-solution is actually lower in energy. In case of

ferromagnetic $Ni_2Mn_{1.4}In_{0.6,}$ the total spin moment from the FP-LAPW calculations was found to be 6.20 μ_B/f.u. which is close to the value (5.51 μ_B/f.u.) reported by Krenke *et al* [14]. Therefore, non-stoichiometric Ni-Mn-In can have ferri- or ferro-state which is expected to depend upon the sample preparation history, extent of antisite disorder, etc. Difference between the spin moments derived from the present MCP or magnetization data and those from the available magnetization data [14, 15] may also be partly due to the slightly different compositions of the specimens used in three different measurements.

4. Conclusions

The temperature dependent MCPs of Ni_2MnIn and $Ni_2Mn_{1.4}In_{0.6}$ have been presented in this paper. MCPs have been analyzed in terms of its Mn 3d and diffuse contributions. The present experimental data on Ni_2MnIn show that at low temperature (10 K) there is a large spin moment (3.60 μ_B) at the Mn site, which is in good agreement with the FP-LAPW band structure calculation. Spin polarized density of states show hybridization between the majority-spin Ni 3d and Mn 3d states, while the minority-spin Ni 3d and Mn 3d states are separated by about 4 eV. The minority-spin Mn 3d states appear above the Fermi level giving rise to large local moment on Mn. In KKR calculations, incorporation of fully relativistic description reproduces smaller value of total spin moment in comparison to FP-LAPW calculations which may be attributed to its CPA mechanism. Our MCP data for $Ni_2Mn_{1.4}In_{0.6}$ (at 10 K) are found to be in reasonable agreement with our SPR-KKR calculations and our magnetization data. Good agreement between the MCP and magnetization total moment shows that the orbital moment contribution is small in Ni-Mn-In system. Significant differences between earlier magnetization data

(reported by Krenke *et al* and Kanomata *et al*) and our data (MCP and magnetization) may be due to thermal history of sample preparation and also slight variation of Mn in the nominal $Ni_2Mn_{1.4}In_{0.6}$ composition. Spin polarized neutron scattering studies, which are also used in determining the change in distribution of magnetic electrons, may also be helpful for comparison with the present theoretical and experimental investigations.

Acknowledgements

The work at SPring8 was performed with the approval of Japan Synchrotron Radiation Research Institute (JASRI) under Proposal No. 2008B-1098. Two of us (BLA + NLH) are grateful to DST, New Delhi and Professor A. K. Raychaudhuri for travel support. DRDO, New Delhi is also thanked for financial assistance. SRB thanks Max Planck Partner group project for financial support.

References

[1] Sutou Y, Imano Y, Koeda N, Omari T, Kainuma R, Ishida K and Oikawa K 2004 *Appl. Phys. Lett.* **85** 4358

[2] Galanakis I, Dederichs P H and Papanikolaou N 2002 *Phys. Rev. B* **66** 174429

[3] Da Silva E Z, Jepsen O and Andersen O K 1988 *Solid State Commun.* **67** 13

[4] Kilian K A and Victora R H 2000 *J. Appl. Phys.* **87** 7064

[5] Godlevsky V V and Rabe K M 2001 *Phys. Rev. B* **63** 134407

[6] Ṣaṣioğlu E, Sandratskil L M and Bruno P 2004 *Phys. Rev. B* **70** 024427

[7] Kudryavtsev Y V, Lee Y P and Rhee J Y 2004 *Phys. Rev. B* **69** 195104

[8] Chakrabarti A and Barman S R 2009 *Appl. Phys. Lett.* **94** 161908
Barman S R, Chakrabarti A, Singh S, Banik S, Bhardwaj S, Paulose P L, Chalke B A, Panda A K, Mitra A and Awasthi A M 2008 *Phys. Rev. B* **78** 134406

[9] Zayak A T, Entel P, Rabe K M, Adeagbo W A and Acet M 2005 *Phys. Rev. B* **72** 054113

[10] Brown P J, Crangle J, Kanomata T, Matsumoto M, Neumann K-U, Ouladdiaf B and Ziebeck K R A 2002 *J. Phys.: Condens. Matter* **14** 10159
Ranjan R, Banik S, Barman S R, Kumar U, Mukhopadhyay P K and Pandey D 2006 *Phys. Rev. B* **74** 224443
Kokorin V V and Chemenko V A 1989 *Phys. Met. Metall.* **68** 111
Zayak A T, Entel P, Enkovaara J, Ayuela A and Nieminen R M 2003 *Phys. Rev. B* **68** 132402

[11] Murray S J, Marioni M, Allen S M, O'Handley R C and Lograsso T A 2000 *Appl. Phys. Lett.* **77** 886
Ullakko K, Huang J K, Kantner C, O'Handley R C and Kokorin V V 1996 *Appl. Phys. Lett.* **69** 1966

[12] Yablonskikh M V, Braun J, Kuchel M T, Postnikov A V, Denlinger J D, Shreder E I, Yarmoshenko Y M, Neumann M and Moewes A 2006 *Phys. Rev. B* **74** 085103

[13] Buchelnikov V D, Entel P, Taskaev V, Sokolovskiy V V, Hucht A, Ogura M, Akai H, Gruner M E and Nayak S K 2008 *Phys. Rev. B* **78** 184427

[14] Krenke T, Acet M, Wassermann E F, Moya X, Mañosa L and Planes A 2006 *Phys. Rev. B* **73** 174413

[15] Kanomata T, Yasuda T, Sasaki S, Nishihara H, Kainuma R, Ito W, Oikawa K, Ishida K, Neumann K U and Ziebeck K R A 2009 *J. Magn. Magn. Mater.* **321** 773

[16] Cooper M J, Mijnarends P E, Shiotani N, Sakai N and Bansil A 2004 *X-ray Compton Scattering* (Oxford: Oxford University Press)
Schulke W 2007 *Electron Dynamics by Inelastic X-ray Scattering* (Oxford: Oxford University Press)

[17] Sakai N 1996 *J. Appl. Crystallogr.* **29** 81

[18] Ahuja B L, Sharma V and Sakurai Y 2008 *Adv. Mater. Research* **52** 145 and references therein
Kakutani Y, Kubo Y, Koizumi A, Sakai N, Ahuja B L and Sharma B K 2003 *J. Phys. Soc. Japan* **72** 599

[19] Zukowski E, Anderjczuk A, Dobrzynski L, Cooper M J, Dixon M A G, Gardelis S, Lawson P K, Buslap T, Kaprzyk S, Neumann K U and Ziebeck K R A 1997 *J. Phys.: Condens. Matter* **9** 10993

[20] Deb A and Sakurai Y 2000 *J. Phys.: Condens. Matter* **12** 2997

[21] Deb A, Itou M, Sakurai Y, Hiraoka N and Sakai N 2001 *Phys. Rev. B* **63** 064409

[22] Deb A, Hiraoka N, Itou M, Sakurai Y, Onodera M and Sakai N 2001 *Phys. Rev. B* **63** 205115

[23] Ahuja B L, Sharma B K, Mathur S, Heda N L, Itou M, Andrejczuk A, Sakurai Y, Chakrabarti A, Banik S, Awasthi A M, and Barman S R, 2007 *Phys. Rev. B* **75** 134403
Ahuja B L, Ahmed G, Banik S, Itou M, Sakurai Y and Barman S R 2009 *Phys. Rev. B* **79** 214403

[24] Rietveld H M 1967 *Acta Cryst. A* **49** 151

[25] Le Bail A, Duroy H and Fourquet J L 1988 *Mater. Res. Bull.* **23** 447

[26] Lobo D N, Priolkar K R, Bhobe P A, Krishnamurthy D and Emura S 2010 *Appl. Phys. Lett.* **96** 232508

[27] Singh S, Maniraj M, D'Souza S W, Ranjan R and Barman S R 2010 *Appl. Phys. Lett.* **96** 081904
Ranjan R, Singh S, Boysen H, Trots D, Banik S, Awasthi A M, Mukhopadhyay P K and Barman S R 2009 *J. Appl. Phys.* **106** 033510

[28] Blaha P, Schwarz K, Madsen G, Kvasnicka D and Luitz J 2001 *WIEN2k* (Vienna, Austria: Vienna University of Technology)
Blaha P, Schwarz K, Sorantin P and Rickey S B 1990 *Comp. Phys. Commun.* 59 399

[29] Perdew J P and Wang Y 1992 *Phys. Rev. B* **45** 13244

[30] Wu Z and Cohen R 2006 *Phys. Rev. B* **73** 235116

[31] Ebert H *et al* version 3.6 *The Munich SPR-KKR Package* http://olymp.cup.uni-muenchen.de/ak/ebert/SPRKKR
Ebert H *Fully Relativistic Band Structure Calculations for Magnetic Solids-Formalism and Application in Electronic Structure and Physical Properties of Solids* Vol. 535 p. 191 (Berlin: Springer)

[32] Vosko S H, Wilk L and Nusair M 1980 *Canadian J. Phys.* **58** 1200

[33] Banik S, Rajan R, Chakrabarti A, Bhardwaj S, Lalla N P, Awasthi A M, Sathe V, Phase D M, Mukhopadhyay P K, Pandey D and Barman S R 2007 *Phys. Rev. B* **75** 104107

[34] Biggs F, Mandelsohn L B and Mann J B 1975 *At. Data Nucl. Data Tables* **16** 201

[35] Dixon M A G, Duffy J A, Gardelis S, McCarthy J E, Cooper M J, Dugdale S B, Jarlborg T and Timms D N 1998 *J. Phys.: Condens. Matter* **10** 2759

[36] Krenke T, Duman E, Acet M, Wassermann E F, Moya X, Manosa L and Planes A 2005 *Nature Mater.* **4** 450

[37] Barman S R, Banik S, Shukla A K, Kamal C and Chakrabarti A 2007 *Europhys. Lett.* **80** 57002
Barman S R and Chakrabarti A 2008 *Phys. Rev. B* **77** 176401

[38] Enkovaara J, Heczko O, Ayuela A and Nieminen R M 2003 *Phys. Rev. B* **67** 212405

Figure captions:

Figure 1: (Color online) Powder X-ray diffraction pattern (dots) along with Le Bail fitting (red line) of (a) $Ni_2Mn_{1.4}In_{0.6}$ and (b) Ni_2MnIn recorded at room temperature. For $Ni_2Mn_{1.4}In_{0.6,}$ the blue ticks represent the Bragg reflections of the $L2_1$ phase and the green ticks (and ´T´) for tetragonal phase. The inset show the exclusively $L2_1$ peaks for $Ni_2Mn_{1.4}In_{0.6}$ in an expanded scale.

Figure 2: (Color online) The band structures of Ni_2MnIn using FP-LAPW (LSDA) scheme. The left and the right hand side panels show (a) majority- and (b) minority- spin bands, respectively. In the majority-spin 31^{st} [T_{1u}, A_2], 32^{nd} [T_{1u}, B_2] and 33^{rd} [T_{1u}, B_1] bands are marked, while in minority-spin the 26^{th} [T_{2g}, B_2], 27^{th} [T_{2g}, B_2] and 28^{th} [T_{2g}, B_1] bands are labeled. The irreducible representations at Γ and K points, respectively, for the marked bands are shown in the square brackets.

Figure 3: (Color online) Spin-projected (↑, ↓) total and partial density of states of Ni_2MnIn using FP-LAPW (LSDA) scheme.

Figure 4: (Color online) Same as figure 2 except the sample, which is $Ni_2Mn_{1.4}In_{0.6}$. For the sake of clarity the energy bands around the E_F region are shown in the insets.

Figure 5: (Color online) Same as figure 3 except the sample, which is $Ni_2Mn_{1.4}In_{0.6}$. Mn(I) and Mn(II) correspond to Mn atoms at Mn sublattice and Mn atom at In site in supercell, respectively.

Figure 6: (Color online) (a) The standard BZ for L_{21} structure with high symmetry directions. FP-LAPW majority-spin (↑) based Fermi surface of Ni_2MnIn arising from (b) 31^{st} [T_{1u}, A_2] (c) 32^{nd} [T_{1u}, B_2] and (d) 33^{rd} [T_{1u}, B_1] bands. In (e) total mapping (b+c+d) is shown. Figures f, g and h correspond to 26^{th} [T_{2g}, B_2], 27^{th} [T_{2g}, B_2] and 28^{th} [T_{2g}, B_1] minority-spin (↓) bands. In square brackets, the irreducible representations at Γ and K points are shown. Part (i) shows complete mapping from all minority-spin surfaces (f+g+h).

Figure 7: Variation of magnetization with temperature [*M*-*T*] under zero field cooled (ZFC), field cooled (FC) and field heated (FH) cycles, measured using SQUID magnetometer at 0.01 T for (a) Ni_2MnIn and (b) $Ni_2Mn_{1.4}In_{0.6}$. In the inset, variation of magnetic effect *R* (at 2.5 T) as defined in Eq. 3 is shown for 10, 175 and 300 K. Solid lines are drawn only to guide the eyes. The order of error is smaller than the size of symbols used.

Figure 8: Spin polarized momentum distribution of (a) Ni_2MnIn and (b) $Ni_2Mn_{1.4}In_{0.6}$ at fixed 2.5 T field and different temperatures decomposed into the Mn 3d, Ni (magnetic, fixed) and diffuse components. The total fit curve (fitted) is shown as a solid line through the data points. Statistical error in MCP data is within the size of symbols used.

Figure 9: (Color online) Temperature dependent magnetic moments determined by the line shape analysis of the magnetic Compton profiles of (a) Ni_2MnIn and (b) $Ni_2Mn_{1.4}In_{0.6}$ measured at 2.5 T field. The solid lines connecting MCP spin moments are drawn only to guide the eyes. Our SQUID data (at 1T saturation field) for $Ni_2Mn_{1.4}In_{0.6}$ is also shown in figure b. The error at Mn site is within the size of symbols used. The spin moment per formula unit (μ_B) is equal to the area under the component curves as shown in figure 8. The value of magnetization (SQUID) data at 5K as reported by Krenke *et al* and Konamata *et al* are also depicted.

Figure 1

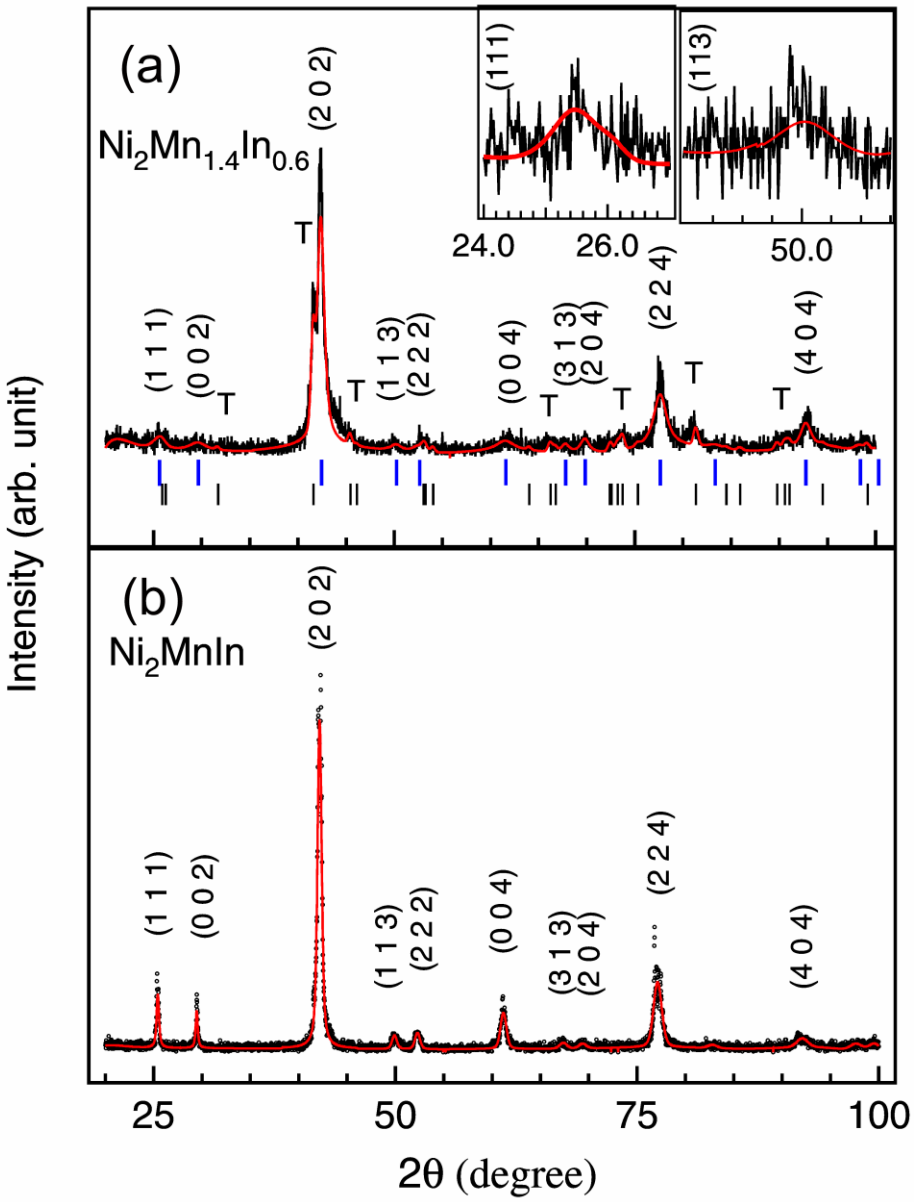
(a)
Ni2Mn1.4In0.6
(2 0 2)
(1 1 1)
(0 0 2)
T
(1 1 3)
(2 2 2)
(0 0 4)
(3 1 3)
(2 0 4)
(2 2 4)
(4 0 4)
(111)
(113)
24.0
26.0
50.0
(b)
Ni2MnIn
Intensity (arb. unit)
25
50
75
100
2θ (degree)

Figure 2

(a) Majority-spin

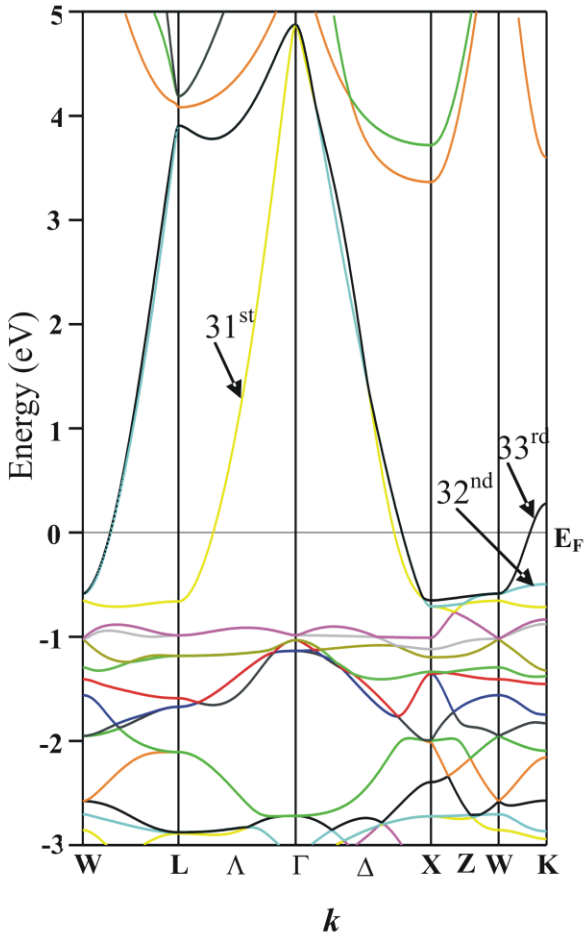

(b) Minority-spin

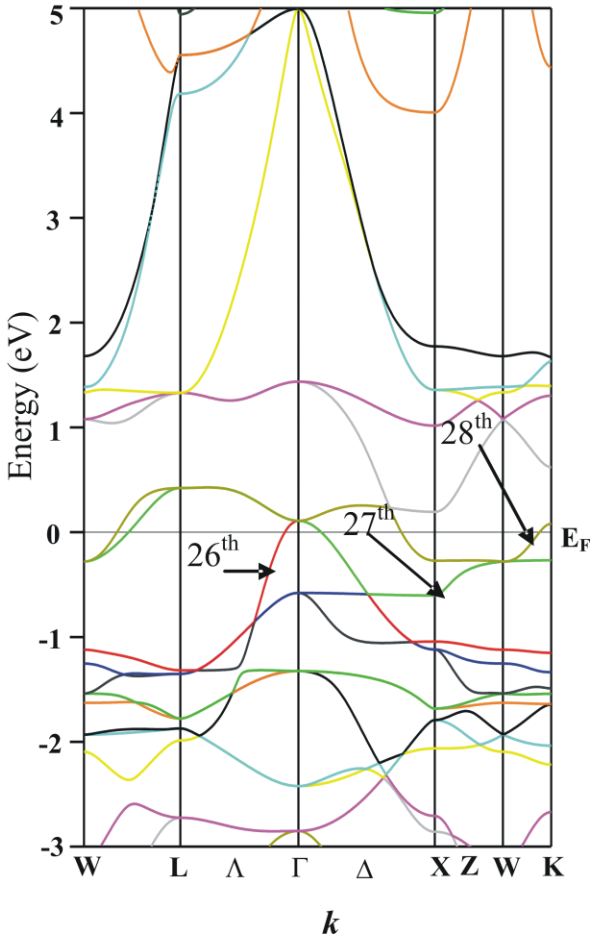

Figure 3

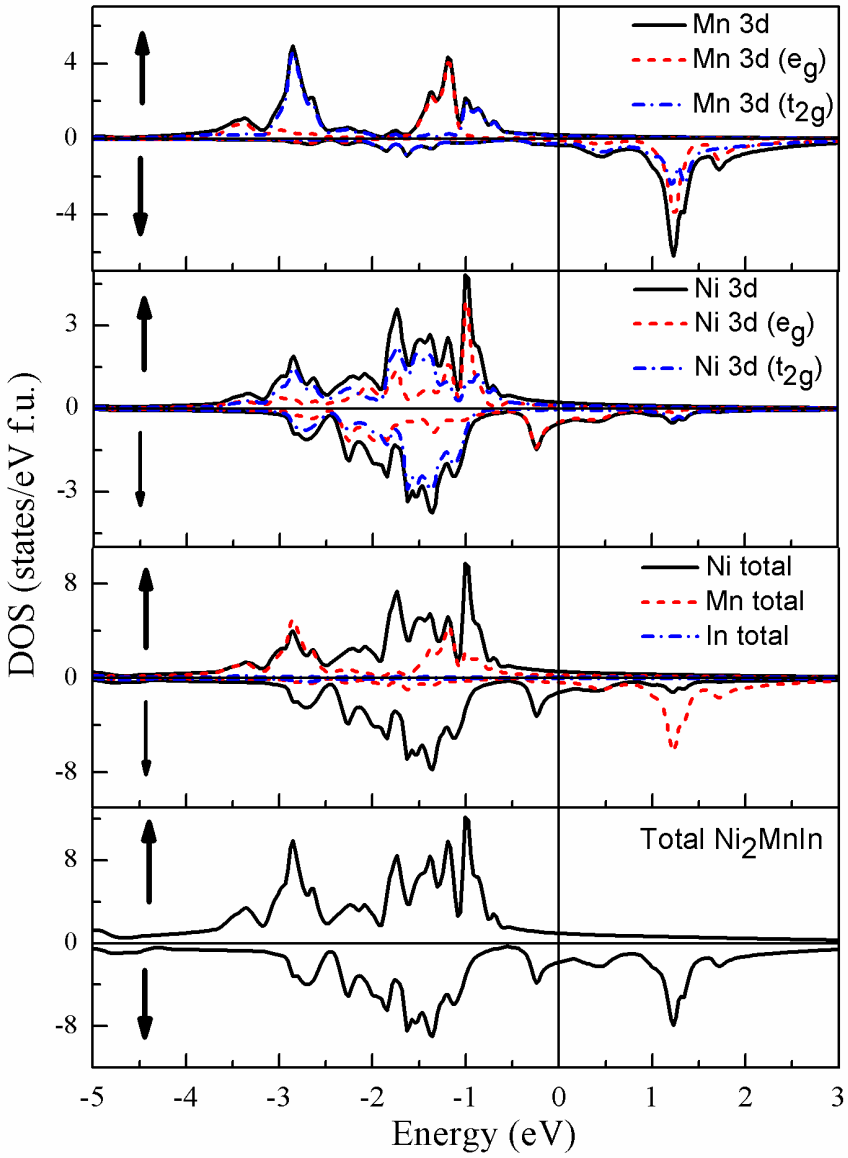
Mn 3d
Mn 3d (eg)
Mn 3d (t2g)
Ni 3d
Ni 3d (eg)
Ni 3d (t2g)
Ni total
Mn total
In total
Total Ni2MnIn
DOS (states/eV f.u.)
Energy (eV)

Figure 4

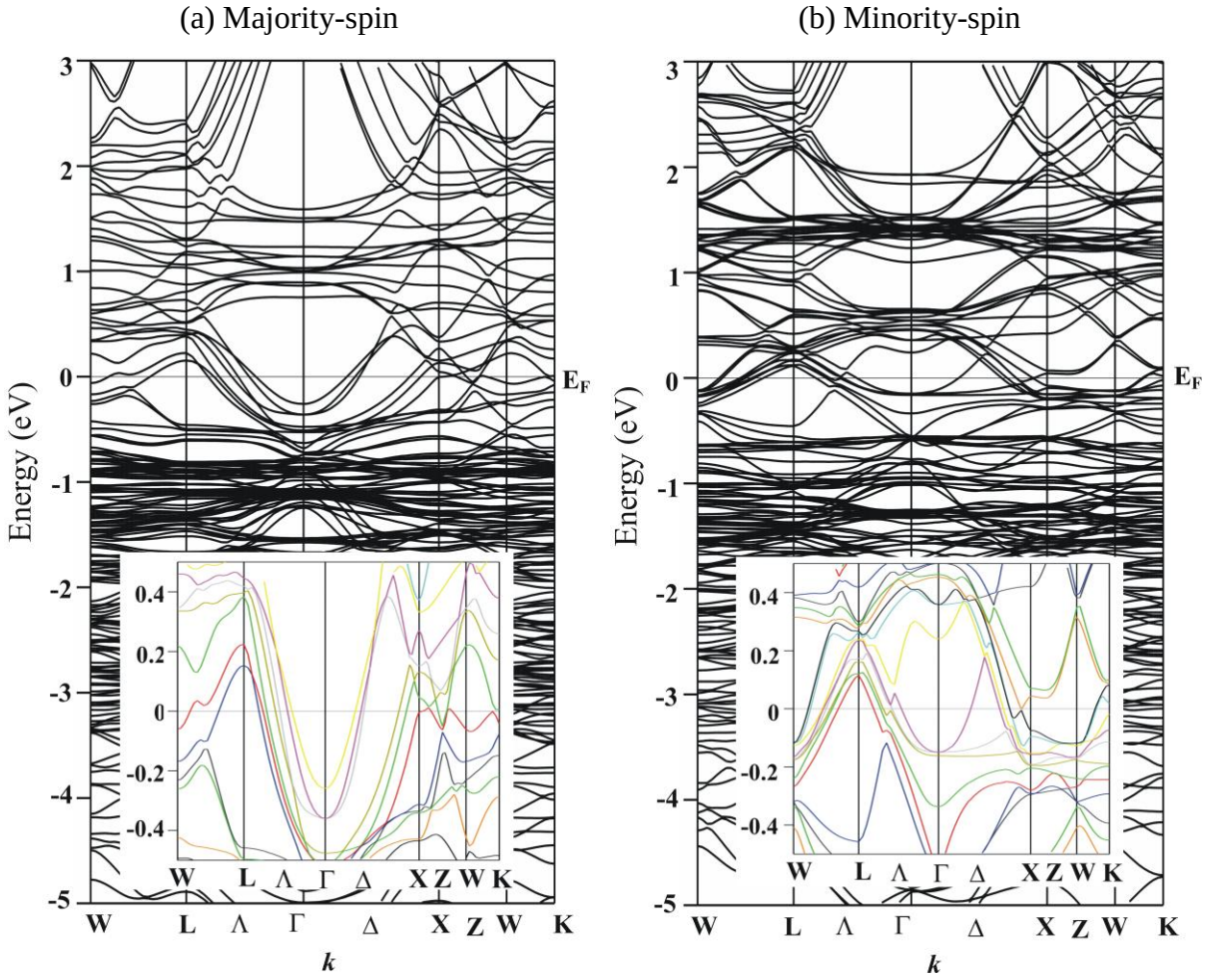

Figure 5

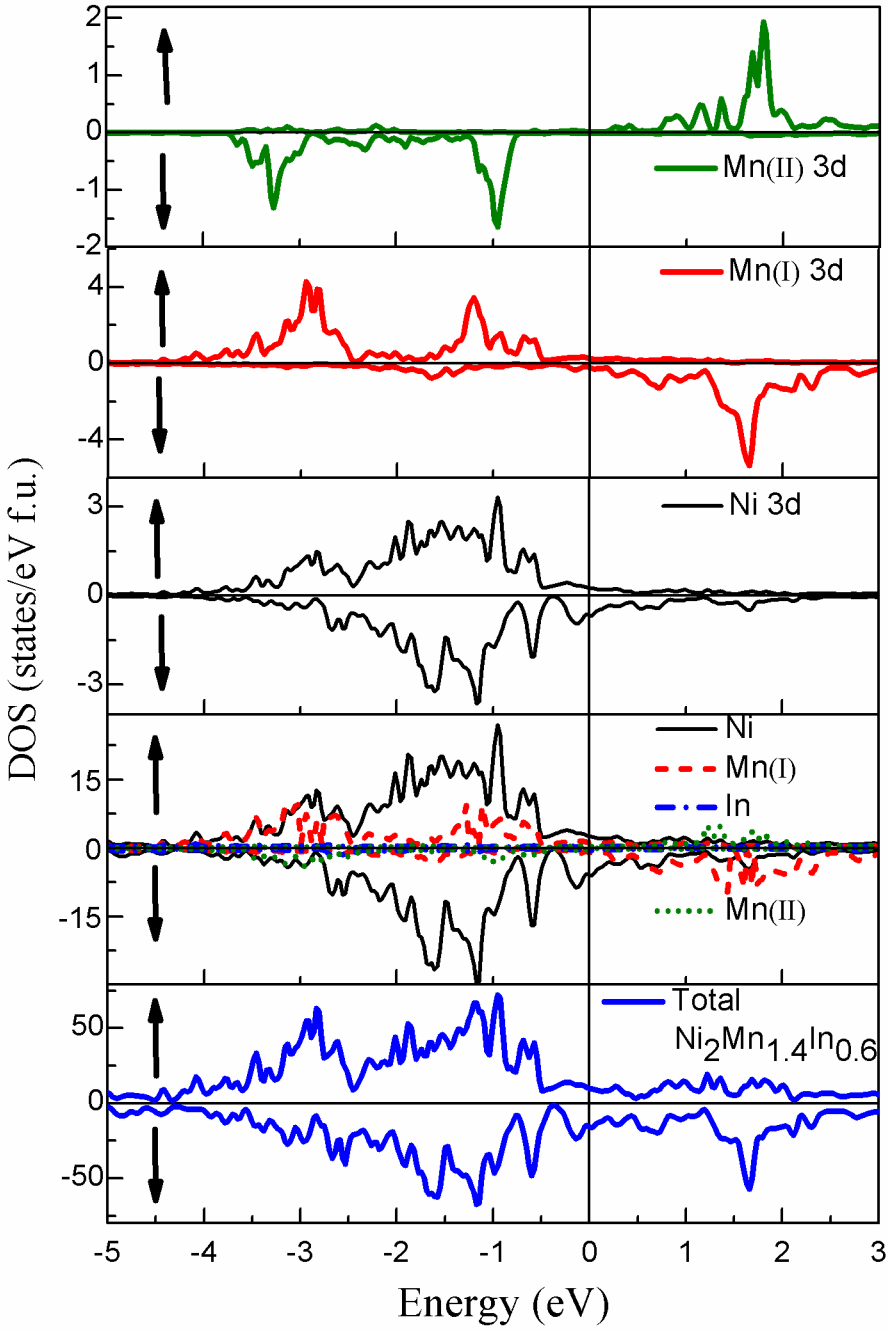
DOS (states/eV f.u.)
Energy (eV)
Mn(II) 3d
Mn(I) 3d
Ni 3d
Ni
Mn(I)
In
Mn(II)
Total
Ni2Mn1.4In0.6

Figure 6

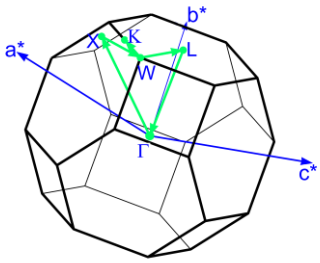

(a) BZ

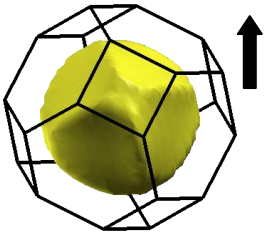

(b) 31st band

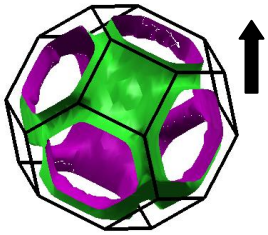

(c) 32nd band

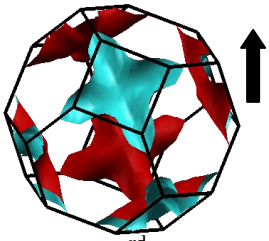

(d) 33rd band

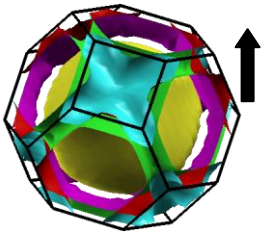

(e) b+c+d

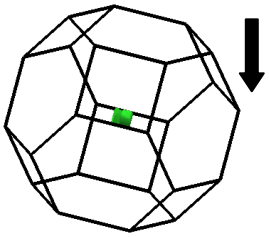

(f) 26th band

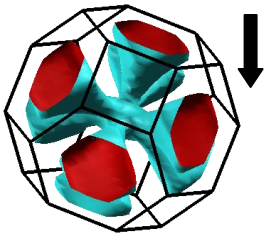

(g) 27th band

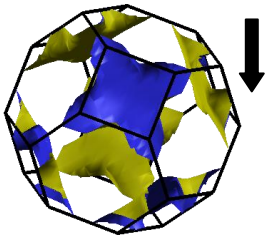

(h) 28th band

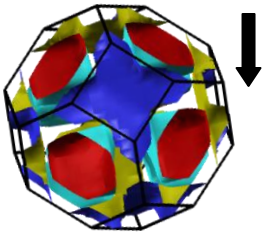

(i) f+g+h

Figure 7

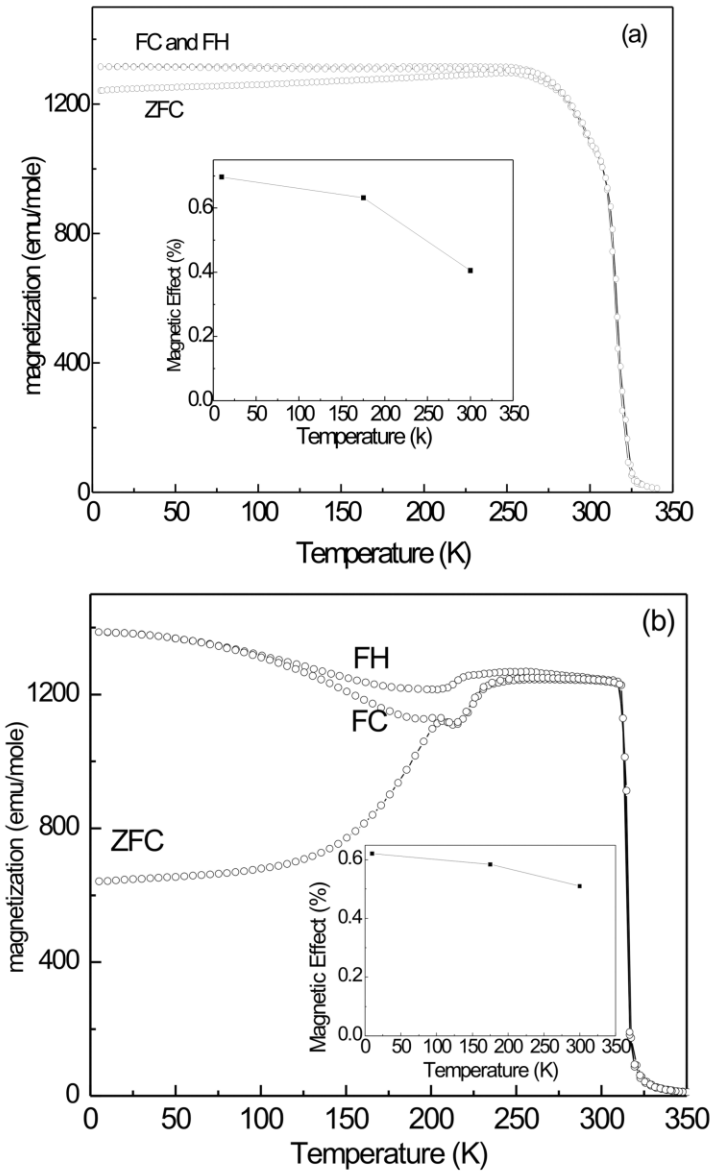
(a)
FC and FH
ZFC
magnetization (emu/mole)
Temperature (K)
Magnetic Effect (%)
Temperature (k)
(b)
FH
FC
ZFC
magnetization (emu/mole)
Temperature (K)
Magnetic Effect (%)
Temperature (K)

Figure 8

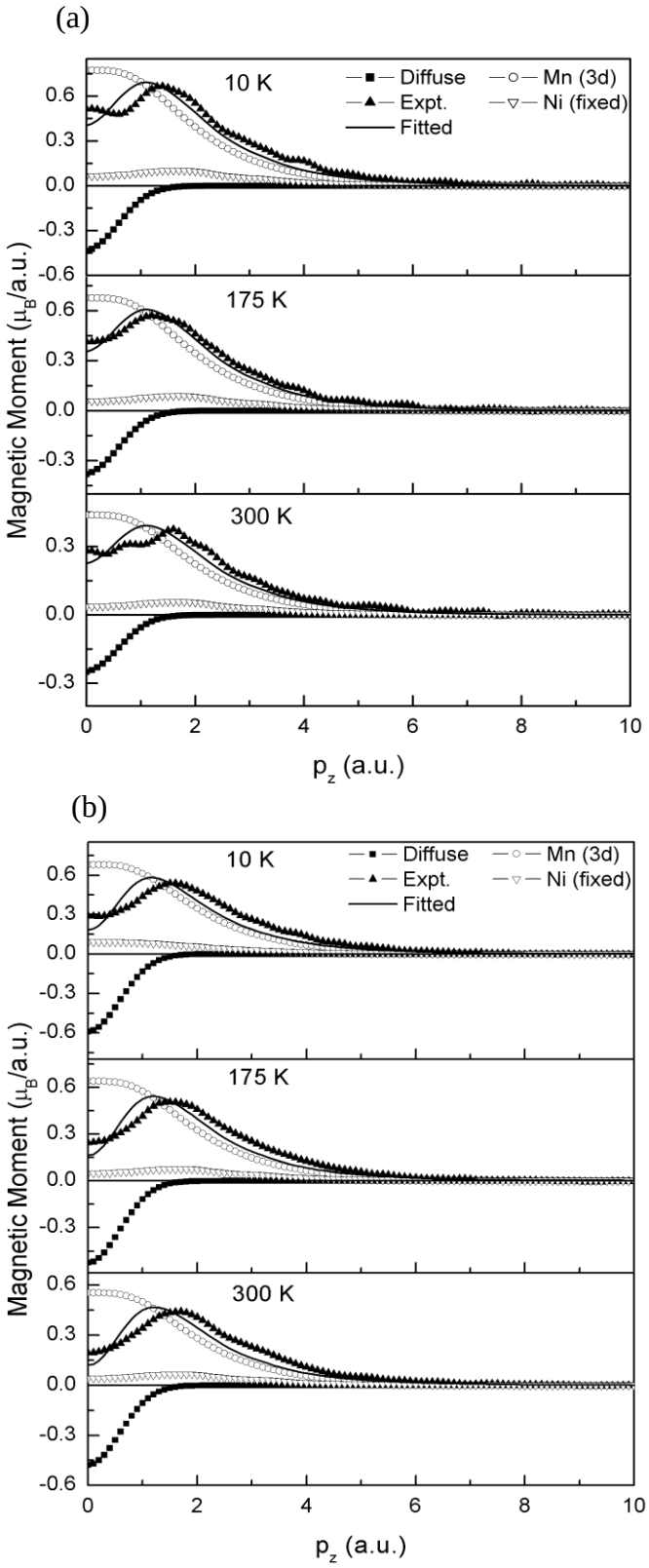
(a)
10 K
175 K
300 K
Diffuse
Expt.
Fitted
Mn (3d)
Ni (fixed)
Magnetic Moment (μ_B/a.u.)
p_z (a.u.)
(b)
10 K
175 K
300 K
Diffuse
Expt.
Fitted
Mn (3d)
Ni (fixed)
Magnetic Moment (μ_B/a.u.)
p_z (a.u.)

Figure 9

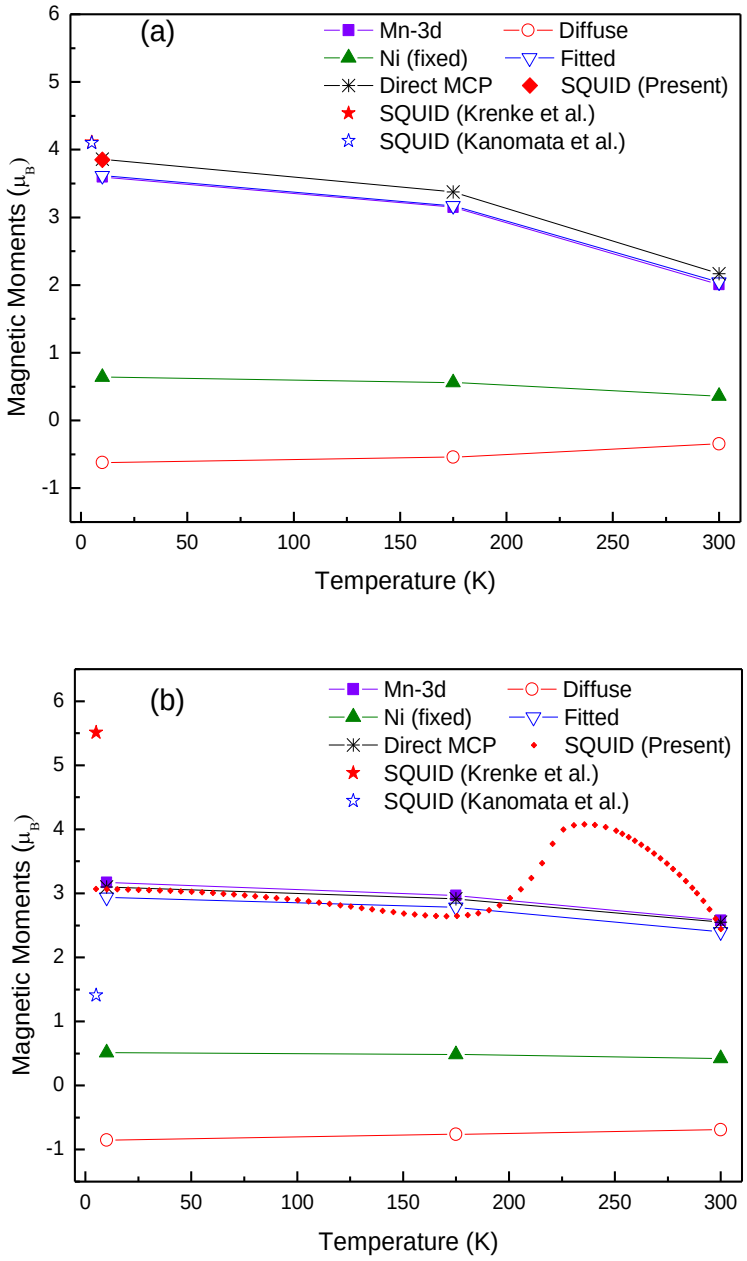
(a)
Mn-3d
Diffuse
Ni (fixed)
Fitted
Direct MCP
SQUID (Present)
SQUID (Krenke et al.)
SQUID (Kanomata et al.)
Magnetic Moments (μ_B)
Temperature (K)
(b)
Mn-3d
Diffuse
Ni (fixed)
Fitted
Direct MCP
SQUID (Present)
SQUID (Krenke et al.)
SQUID (Kanomata et al.)
Magnetic Moments (μ_B)
Temperature (K)

Table 1: Local spin magnetic moments and average local spin moments for each atom type for Ni_2MnIn and $Ni_2Mn_{1.4}In_{0.6}$ calculated using FP-LAPW calculations. Multiplicity of different atomic sites is also given. All moments are given in μ_B. In both the compositions the R_{MT} was kept as 2.47, 2.47 and 2.40 a.u. for Ni, Mn and In, respectively.

Definition	Constituent atom	Multiplicity	Local moment for inequivalent atoms	Average local moment for each atom type	Average moment for each atom type/ f.u.	Total moment μ_B/fu.
(i) Ni_2MnIn (ferromagnetic)	Ni	2	0.32	0.32	0.64	4.10
	Mn	1	3.50	3.50	3.50	
	In	1	-0.04	–0.04	–0.04	
	Interstitial				0.001	
(ii) $Ni_2Mn_{1.4}In_{0.6}$ (ferrimagnetic)	Ni1	8	0.33	0.29	0.57	2.65
	Ni2	8	0.24			
	Mn(I)1	4	3.56	3.58	3.58	
	Mn(I)2	2	3.59			
	Mn(I)3	2	3.62			
	In1	4	-0.03	–0.03	–0.018	
	In2	1	-0.03			
	Mn(II)1	1	-3.70	–3.70	–1.48	
	Mn(II)2	2	-3.70			
	Interstitial				0.01	

Table 2: The spin magnetic moments of Ni_2MnIn and $Ni_2Mn_{1.4}In_{0.6}$ using FP-LAPW and SPR-KKR schemes along with the available theoretical data.

	Magnetic moment (in μ_B/f.u.)				Salient aspects of calculation
	2xNi site	Mn site	In site	Total	
(i) Ni_2MnIn					
Present work					
(a) FP-LAPW (LSDA)	0.64	3.50	−0.04	4.10	WIEN2K, R_{MT} (a.u.): Ni=2.47,
FP-LAPW (GGA)	0.64	3.59	−0.04	4.19	Mn=2.47, In=2.40
(b) SPR-KKR with CPA (VWN)	0.60	3.42	−0.08	3.94	Green function method with touching MT spheres
Available data					
(a) LMTO[a] [3]	−	3.43	−	3.91	ASA[f], von Barth Hedin, R_{MT} not mentioned
(b) LASTO[b] [4]	−	3.51	−	4.09	LDA, Slater type orbital, R_{MT} not mentioned
(c) LSD-PP[c] [5]	−	−	−	4.31	Troullier martins PP, Cutoff radii for PP (a.u.): Ni=2.2, Mn=2.0, In=3.0
(d) ASW[d] [6]	0.56	3.72	−0.07	4.21	ASA[f], GGA, radii of all spheres equal
(e) DFT-GGA (VASP code) [9]	−	−	−	4.22	Kinetic energy cutoff 337.3 eV
(f) FP-LAPW (GGA) [12]	0.70	3.44	−0.02	4.12	WIEN2K, R_{MT} not mentioned
(ii) $Ni_2Mn_{1.4}In_{0.6}$					
Present work					
(a) FP-LAPW (LSDA)	0.57	2.10	-0.02	2.65	WIEN2K, R_{MT} (a.u.): Ni=2.47,
FP-LAPW (GGA)	0.55	2.10	-0.03	2.62	Mn=2.47, In=2.40
(b) SPR-KKR with CPA (VWN)[e]	0.66	2.49	-0.02	3.13	Green function method with touching MT spheres

[a]LMTO: Linear combination of muffin-tin orbitals
[b]LASTO: Linearized augmented Slater type orbitals
[c]LSD-PP: Local spin density with pseudopotential approach
[d]ASW: Augmented spherical wave
[e]VWN: Vosko-Wilk-Nusair
[f]ASA: Atomic sphere approximation